

A Hybrid Solar Absorber–Electrocatalytic N-Doped Carbon/Alloy/Semiconductor Electrode for Localized Photothermic Electrocatalysis

Fan Lu Meng, Gamze Yilmaz, Tian Peng Ding, Minmin Gao, and Ghim Wei Ho*

Converting and storing intermittent solar energy into stable chemical fuels of high efficiency depend crucially on harvesting excess energy beyond the conventional ultraviolet light spectrum. The means of applying highly efficient solar–thermal conversion on practical electricity-driven water splitting could be a significant stride toward this goal, while some bottlenecks remain unresolved. Herein, photothermic electrocatalytic oxygen and hydrogen evolution reactions are proposed, which bestow a distinctive exothermic activation and electrochemical reactivity in a reconstructed electrolyzer system, and which are poised for efficient renewable energy production. Attributed to the synergistic in situ coupling of the N-doped carbon, metallic alloy and oxides, in view of their broadband light absorption, high electrochemical surface area, and efficient charge transfer attributes, the hybrid photothermal electrocatalytic electrode simultaneously satisfies efficient photon-to-heat conversion and augmented electrochemical catalytic activity. Finally, a system level design of an appropriate photothermally mediated electrolytic cell with close-proximity light-illumination window along with a low-thermal-emittance electrolyte separator that preserve an overall large localized thermal gradient and efficient mass transport is devised. Such a photothermally mediated electrocatalytic system presented here may open up new avenues for the development of solar–thermal energy utilization in other forms.

Solar energy harvesting and utilization offers a promising pathway to alleviate energy crisis and environmental pollution issues toward the realization of sustainable development. Over the past decades, diverse technologies such as photovoltaics, photosynthesis, and photothermal conversion have been developed.^[1–5] Water splitting using sunlight, based on the aforementioned technologies provides an appealing approach to convert and store abundant yet intermittent solar energy into storable,

and transportable renewable hydrogen fuel and valuable chemical feedstock. In view of this notion, photochemical, photoelectrochemical, and photovoltaic-driven electrochemical catalytic hydrogen and oxygen evolution are extensively studied.^[6–10] Though photocatalysis involves direct conversion, it suffers from low solar energy absorption and conversion efficiency, the use of sacrificial agents, slow reaction rate, and instability.^[11–14] To overcome these obstacles, photoelectrochemical strategy is explored as it holds the promise of a more efficient means.^[14] Even that, it is hampered by the adversaries of semiconductor catalysts selection, photoelectrode preparation, limited spectral absorption, unsatisfactory reactivity and solar conversion efficiency.^[13] Then, a roundabout way of photovoltaic-driven electrochemical water splitting via alkaline water electrolyzers was considered.^[10,15] The technology can achieve a solar conversion efficiency over 15%, which is highly competitive, let alone the benefits of program controllability, sustainable productivity, and system upgradability with cheaper and more efficient photovoltaic cells.^[15,16] Still, further efficiency improvement can be expected since the overall efficiency of electrochemical splitting of water is hindered by the inherent thermodynamics and sluggish kinetics, including high overpotential, low current density, and moderate energetic efficiency.^[17–22] Despite immense efforts in designing various composition and structure to optimize the intrinsic activity of catalysts, the progress remains insufficient.

Recently, supplementing thermal energy to perform catalytic conversion and vaporize water to surpass the conventional performances is attracting more attention.^[23–28] Rationally, capitalizing the full potential of solar energy, beyond the limitation of UV light excitation, that are not absorbed by photocatalyst or photovoltaic cells for water splitting will undoubtedly augment the efficiency to further accelerate technological deployment. Hence the introduction of photothermal energy to electrochemical reaction can be a feasible pathway to facilitate enhanced solar energy conversion to chemical fuels. However, the biggest challenge lies in the discordant solar absorber electrode and electrolytic cell design. Typically, the catalyst is constructed in a form of film electrode, infiltrated

Dr. F. L. Meng, Dr. G. Yilmaz, Dr. T. P. Ding, Dr. M. Gao, Prof. G. W. Ho
Department of Electrical and Computer Engineering National University
of Singapore
4 Engineering Drive 3, Singapore 117583, Singapore
E-mail: elehgw@nus.edu.sg

Prof. G. W. Ho
Institute of Materials Research and Engineering
A*STAR (Agency for Science, Technology and Research)
2 Fusionopolis Way, Innovis, Singapore 138634, Singapore

 The ORCID identification number(s) for the author(s) of this article can be found under <https://doi.org/10.1002/adma.201903605>.

DOI: 10.1002/adma.201903605

in the bulk electrolyte. This will inevitably cause considerable heat losses to bulk electrolyte by rapid thermal diffusion, hence leading to poor photothermal utilization.^[29–33] Consequently, the highly promising photothermal effect was not duly exploited to unleash a maximum impact on the electrocatalytic performance.

Herein, we report a successful design of a collegial photothermal electrode–electrolyzer for an electrolytic system which is well-suited for distributed hydrogen production that is coupled to the solar renewable source. Essentially, a photothermal electrocatalytic system for water splitting consisting of a hybrid solar absorber and electrocatalyst operating in a remodeled water electrolyzer for localized photoheating, has been constructed to realize high efficiency solar energy conversion to chemical fuels. A 3D array of N-doped carbon nanotubes/mixed metallic structure electrode is fabricated through a one-step in situ reduction and chemical vapor deposition (CVD) strategy, with judicious introduction of carbon functioning as a broadband light absorbing material and conductive transition metals serving as efficient electrocatalysts. Such hybrid electrode demonstrates full solar harvesting and conversion in two distinctive mechanisms, i.e., semiconductor photoexcitation and solar–thermal energy conversion to boost water splitting through combinative photon–phonon mediated catalysis. Meanwhile, the re-designed photothermal electrocatalysis cell, i.e., an electrolyzer with proximal electrode light access and low thermal emission porous foam inclusion is proven to effectively suppress the rapid heat losses and localize the photothermal heat without compromising the superior mass transport of the redox species. Consequently, these synergistic hybrid solar absorber–electrocatalytic electrode and reactor infrastructure design enables dramatically low overpotential and fast kinetics both for the hydrogen and oxygen evolution reactions (HER and OER), suggesting a feasible approach to increase the utilization of solar energy for renewable energy powered hydrogen production.

The integrated 3D carbonaceous/metallic hybrid array structure (CM/TiO_{2-x}/CP) is prepared through a simultaneous in situ thermal reduction and CVD approach using mixed metal oxides (Fe-doped NiO and TiO₂) template and melamine precursor to facilitate spontaneous generation of nitrogen/carbon-rich reductive reaction environment. **Figure 1a** illustrates the multistep preparation process of the CM/TiO_{2-x}/CP, which involves hydrothermal growth of TiO₂ nanoneedles array on a carbon paper substrate (denoted as TiO₂/CP) (Figure S1, Supporting Information), deposition of Fe-doped NiO nanosheets on TiO₂ nanoneedles (denoted as MO/TiO₂/CP) (Figure S2, Supporting Information), followed by subsequent thermal reduction and alloy-catalyzed N-CNTs growth that leverages on the pyrolysis of melamine under flowing argon (Ar) gas. The morphology and structure evolution is examined using scanning electron microscopy (SEM) and transmission electron microscopy (TEM). As shown in Figure 1b,c, the N-CNTs are loosely interconnected with each other and intertwined with the original core nanoneedles, engendering a highly macroporous structure with copious internal spaces. Notably, the alignment of the microstructure is well preserved after the multistep synthetic route. TEM image in Figure 1d further shows that loosely packed and long N-CNTs extend radially from all sides of the rough nanoneedle, transforming

the original smooth oxide nanosheets/TiO₂ nanoneedle into a new CM/TiO_{2-x} core/shell structure. High-magnification TEM (HRTEM) images in Figure 1e,f show lattice fringes with interplanar spacings of 0.205, 0.209, and 0.324 nm, which correspond to the (111) plane of awaruite Ni₃Fe,^[34] (200) plane of cubic TiO,^[35] and (111) plane of rutile TiO₂,^[36] respectively. The CNTs exhibit a multiwall structure with a diameter of about 34.6 nm, which have nucleated and grown from the abundant Ni₃Fe nanoparticles decorated TiO_{2-x}. Moreover, high-angle annular dark field scanning transmission electron microscopy (HAADF-STEM) analysis (Figure 1g) and element mapping probe the existence of Ti, Ni, Fe, N, O, and C elements, and reveal uniform spatial distributions of alloy nanoparticles, CNTs, and TiO_{2-x} nanoneedles. This conversion process not only indicates the scaffold role of TiO₂ nanoneedle to support the whole core/shell–based array configuration, but also reveals the base-growth of N-CNTs catalyzed by the Ni₃Fe alloy nanoparticles deposited on TiO₂ nanoneedles. Importantly, the interfacial nanoassembly of N-CNTs, FeNi alloy, and TiO_{2-x} can induce favorable electronic coupling effects, enrich active sites density, and favor a high charge flux and thermal transfer.^[37–39] For comparison, TiO_{2-x}/CP and CM/CP derived from TiO₂/CP and MO/CP by melamine assisted thermal reduction or CVD are also synthesized, respectively. After thermal treatment, TiO_{2-x}/CP retains the integrity of nanoneedle array structure, while arising coarse surfaces and disappeared tips (Figure S3, Supporting Information). A typical HRTEM image of TiO_{2-x}/CP confirms the presence of mixed cubic TiO and rutile TiO₂ phases and nanopores confined in these two different particles. The nanopores are resulted from the chemical etching by the reductive nitrogen/carbon gas that is released by the decomposition of melamine. For CM/CP, though a large number of intertwining N-CNTs are formed, they are seen to adversely delaminate or peel off from the carbon fiber (Figure S5, Supporting Information). This in turn demonstrates that TiO₂ nanoneedles play a vital function for the formation of strongly integrated and anchored microstructures.

X-ray diffraction (XRD) is carried out to investigate the crystal structures of the samples fore-and-aft heat treatment. Multiple peaks in XRD patterns of CM/TiO_{2-x}/CP (**Figure 2a**) match well with the pure awaruite Ni₃Fe (PDF-# 38-0419), and cubic TiO (PDF-# 08-0117), except for the diffraction peaks of TiO₂ and carbon, which are consistent with the TEM results, indicating successful transformation to carbon/alloy/semiconductor hybrid from original oxides (Figure S6, Supporting Information). X-ray photoelectron spectroscopy (XPS) is used to probe the chemical structure of the samples. Apart from the Ni⁰ and Fe⁰ of Ni₃Fe alloy, metal oxides are also observed in the high-resolution XPS spectra of Fe 2p_{3/2}, and Ni 2p_{3/2} owing to the inevitable partial oxidation on surface under air atmosphere (Figure S7a,b, Supporting Information).^[37,40] The high-resolution spectrum of C 1s of CM/TiO_{2-x}/CP can be deconvoluted into two peaks, namely, C–C (284.5 eV) and C=N (285.6 eV),^[41] suggesting the successful nitrogen doping into the carbon framework (Figure S7c, Supporting Information). Moreover, pyridinic-N (398.7 eV) and graphitic-N (400.9 eV) peaks detected in the high resolution N 1s spectrum (Figure S7d, Supporting Information) further confirm the types of the nitrogen atom bonding within the CNTs.^[42] Comparing the

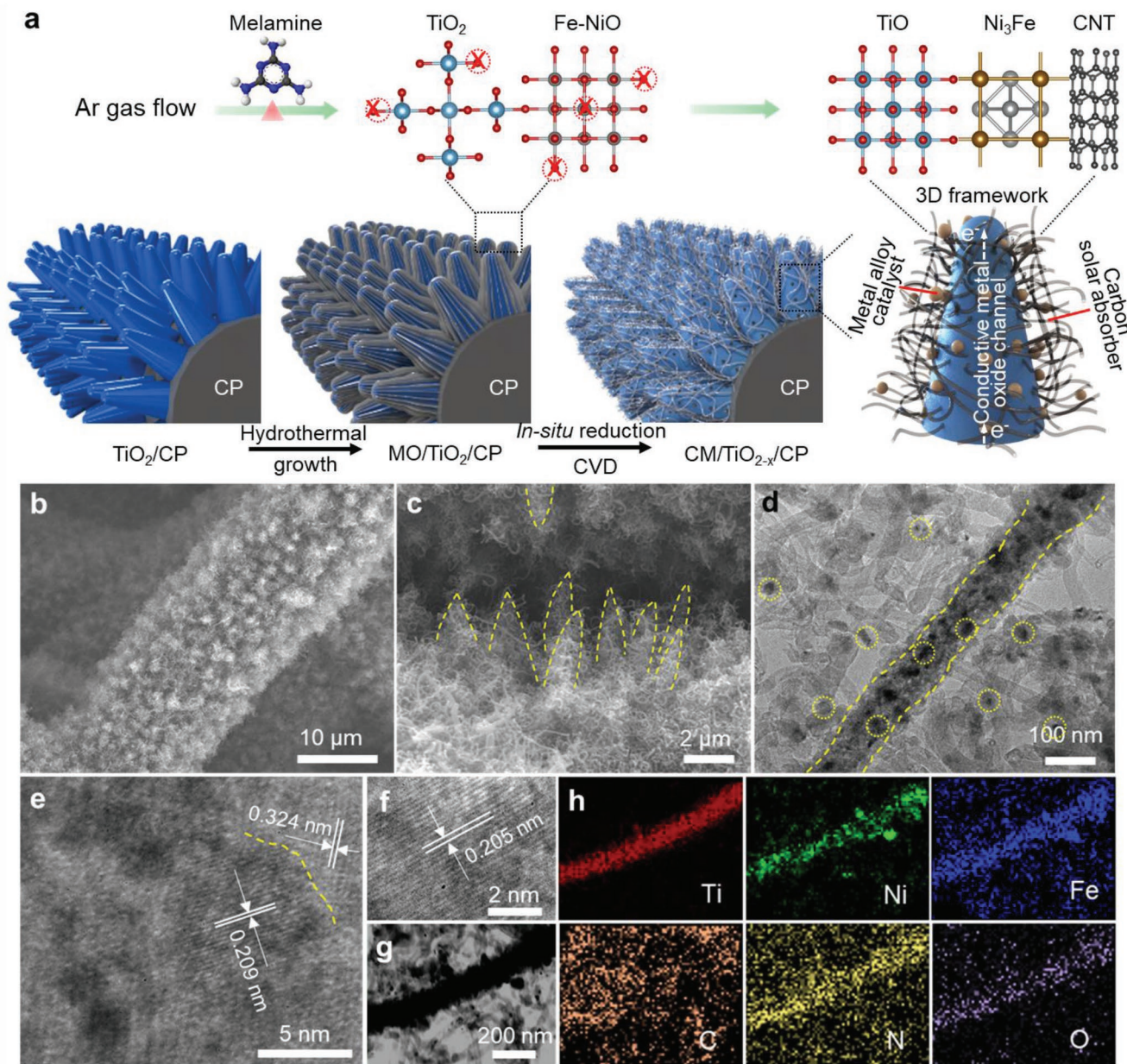


Figure 1. a) Schematic diagram of preparation of CM/TiO_{2-x}/CP. b,c) Low- and high-magnification SEM images of CM/TiO_{2-x}/CP. d) TEM and e,f) HRTEM images of CM/TiO_{2-x}/CP. g) HAADF-STEM image of the CM/TiO_{2-x}/CP, and h) the corresponding elemental mapping images for Ti, Ni, Fe, C, N, and O elements.

Ti 2p XPS spectra of CM/TiO_{2-x}/CP, reduced chemical state from TiO₂ to TiO can be observed (Figure 2b).^[43,44] Density functional theory (DFT) calculations are performed to investigate the electronic structures of TiO and TiO₂. The calculated density of states (DOS) across the Fermi level (Figure 2c) demonstrates that TiO exhibits metallic character compared to TiO₂ with a bandgap energy of around 3.0 eV, resulting in a more efficient electron transfer. Moreover, UV-vis-NIR diffuse reflectance spectroscopy is employed to examine the absorption characteristics of the samples. The CM/TiO_{2-x}/CP exhibits extremely low light reflectance ($\approx 3\text{--}5\%$) in full solar spectrum regions in comparison with MO/TiO₂/CP, TiO₂/CP, and CP,

rendering it a promising solar absorbing material (Figure 2d). Surprisingly, TiO_{2-x}/CP and CM/CP present similar spectral characteristics. As shown in Figure 2e,f, under simulated one sun irradiation (100 mW cm^{-2}), the temperature of the CM/TiO_{2-x}/CP rapidly rises from 22 to 87.8 °C in 10 min, while TiO_{2-x}/CP and CM/CP attain slightly lower temperatures of 83.1 and 84.3 °C. In contrast, the temperatures of MO/TiO₂/CP, TiO₂/CP, and CP are below 70 °C. Meanwhile, under UV light irradiation, the CM/TiO_{2-x}/CP displays much lower temperature increase (Figure S8, Supporting Information). These data suggest that marked temperature increase could stem from an efficient vis-NIR photo-to-thermal conversion.^[45]

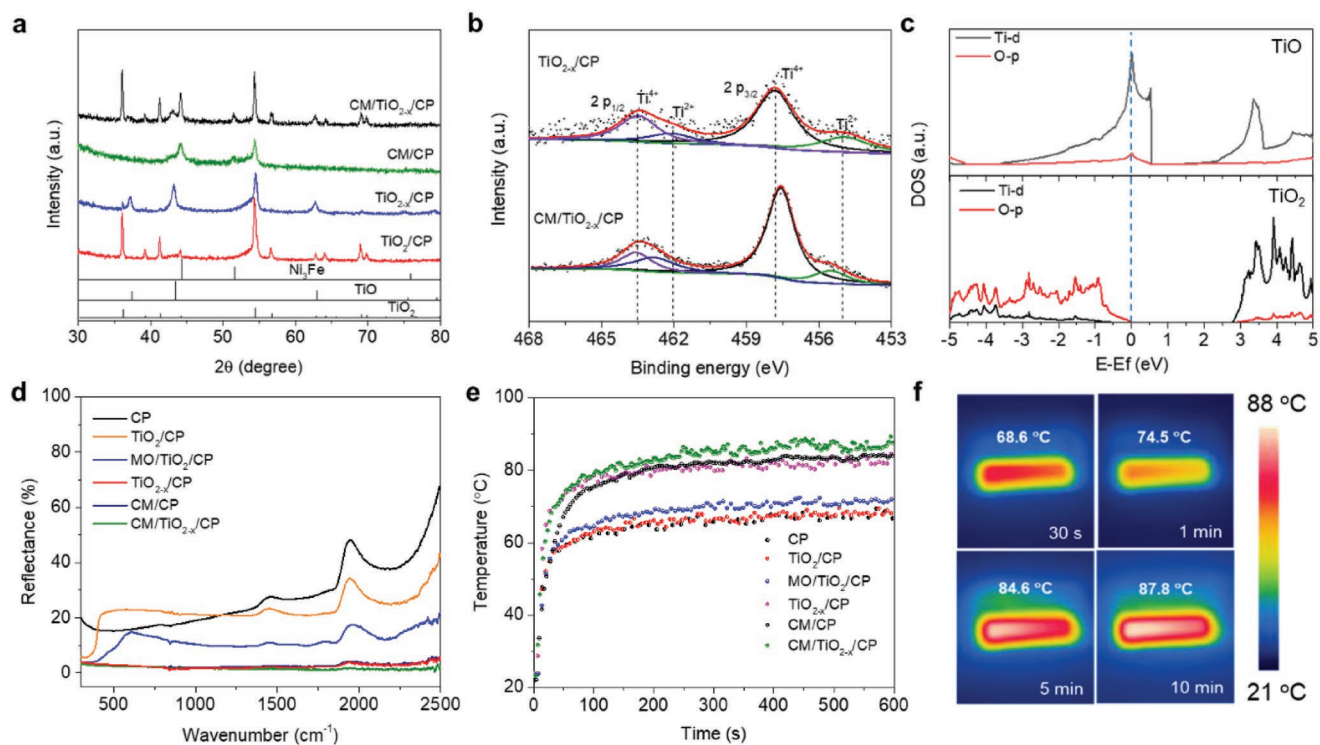


Figure 2. a) XRD patterns of CM/TiO_{2-x}/CP, CM/CP, TiO_{2-x}/CP, and TiO₂/CP. b) XPS spectra for Ti 2p of CM/TiO_{2-x}/CP, and TiO_{2-x}/CP. c) Density of states for TiO and TiO₂. The Fermi level is set at 0 eV. d) UV-vis-NIR absorption spectra of the pristine CP, TiO₂/CP, and MO/TiO₂/CP, and thermal treated samples of CM/CP, TiO_{2-x}/CP, and CM/TiO_{2-x}/CP and e) related temperature evolution; f) infrared images of CM/TiO_{2-x}/CP under simulated one sun light irradiation.

which are attributed to the covering N-CNTs, reduced chemical state from TiO₂ to TiO, and hierarchical nanoarray structure for multiple reflections of the incident light.

Initially, the HER and OER activities of the CM/TiO_{2-x}/CP are first evaluated in 1 M KOH electrolyte using a three-electrode electrochemical configuration. The MO/TiO₂/CP, TiO_{2-x}/CP, CM/CP, and CP are also tested for comparison. Impressively, as for OER, the potential applied on the CM/TiO_{2-x}/CP to deliver the current density of 10 mA cm⁻² is 1.47 V, which is much more negative than that of the MO/TiO₂/CP (1.56 V) and CM/CP (1.51 V) (Figure 3a). The CM/TiO_{2-x}/CP exhibits a much lower overpotential (η) of 142.8 mV to achieve the current density of 10 mA cm⁻² in the HER process, as compared with CM/CP ($\eta = 250.9$ mV), and the pure metal oxide-based MO/TiO₂/CP ($\eta = 258.5$ mV) (Figure 3c). Both OER and HER activities of CM/TiO_{2-x}/CP are comparable to the recently reported hybrid carbon/transition metal electrocatalysts (Tables S1, S2, Supporting Information). Notably, the carbon paper substrate and TiO_{2-x} arrays contribute negligibly to the OER and HER activity, indicating that nickel-iron species and N-doped CNTs are dominantly responsible for the high HER and OER activity. This further confirms the importance of in situ coupling of N-CNTs and reduction of the electrocatalyst into metallic alloy and TiO constituents. The catalytic kinetic activities of the electrocatalysts are evaluated using the Tafel plots (Figure 3b,d). The CM/TiO_{2-x}/CP possesses prominently smaller Tafel slopes for both HER (56.7 mV dec⁻¹) and OER (67.1 mV dec⁻¹) compared to those of the MO/TiO₂/CP

(168.1 and 87.6 mV dec⁻¹ for HER and OER, respectively) and CM/CP (127.8 and 130.6 mV dec⁻¹ for HER and OER, respectively), indicating highly favorable reaction kinetics toward oxygen and hydrogen evolution. In view of practical use, long-term stability of the CM/TiO_{2-x}/CP for continuous oxygen and hydrogen production is another critical parameter besides low overpotential requirement and fast reaction kinetics. In this regard, constant operating potentials required to drive a multi-current step of intermittent 10 and 20 mA cm⁻² for 30 h are implemented to chronoamperometric tests. Figure 3e clarifies that the CM/TiO_{2-x}/CP possesses robust HER and OER durability in alkaline media, in which, the overpotential for OER only increases about 13.8% (243.9–277.5 mV), and shows negligible change for HER after consecutive operations. The degradation in OER activity may be attributable to the partial oxidation of N-CNTs on the CM/TiO_{2-x} nanoarray structure under oxidizing potential.^[46,47] This is verified by the apparent damage of CNTs wrapped on TiO_{2-x} nanoneedles presented in SEM and TEM images (Figure S9, Supporting Information) and weak diffraction peaks for Ni₃Fe of CM/TiO_{2-x}/CP (Figure S11, Supporting Information). Further XPS characterization after the long-term OER operation reveals the new oxidation state of O=C–OH (Figure S12a, Supporting Information), and higher oxidation state of the nickel-iron species (Figures S13b and S14b, Supporting Information). This could be ascribed to a commonly observed surface oxidation of transition-metal-based catalysts during the OER process, which transpires as the actual OER active sites as reported by the earlier works.^[17,48–50] More interestingly,

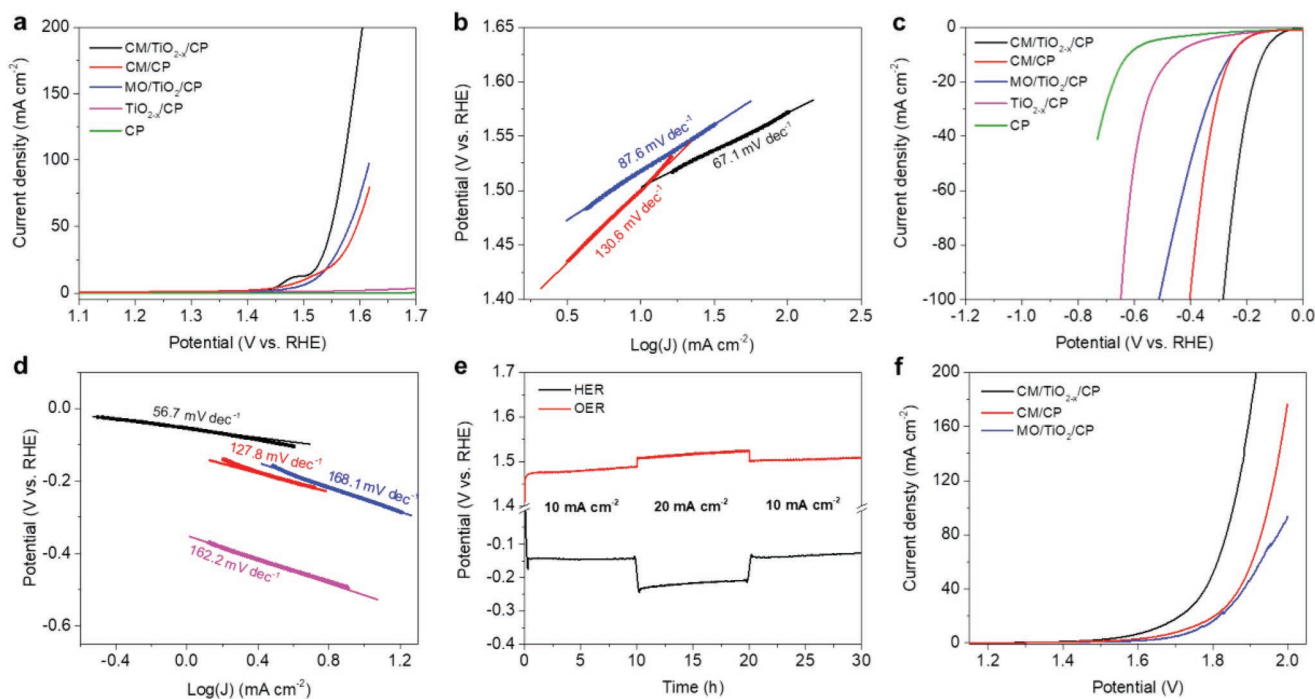


Figure 3. Electrochemical activities toward OER and HER of CM/TiO_{2-x}/CP, CM/CP, TiO_{2-x}/CP, MO/TiO₂/CP, and CP. a) OER polarization curves, and b) corresponding Tafel plots. c) HER polarization curves, and d) corresponding Tafel plots. e) Galvanostatic OER and HER stability test of CM/TiO_{2-x}/CP. f) Two-electrode polarization curves.

the CM/TiO_{2-x}/CP reserves metallic TiO (Figure S15b, Supporting Information), further indicating the faster electron transport and nanoarray structure stability throughout the process. After the HER stability test, CM/TiO_{2-x}/CP maintains the original morphology (Figure S10, Supporting Information), and shows negligible elemental state changes as seen from the XPS spectra (Figures S12–S15, Supporting Information), suggesting its stable chemical and morphological nature.

To uncover the advantageous traits of CM/TiO_{2-x}/CP for superior HER and OER activities, electrochemical active area (ECSA) is first evaluated by electrochemical double-layer capacitance (C_{dl}) measurements at the solid–liquid interface to estimate the accessible active sites.^[51] As shown in Figures S16–S19 (Supporting Information), C_{dl} of the CM/TiO_{2-x}/CP is measured to be 247.8 and 213.1 mF cm⁻² for HER and OER, respectively, which are much higher than those of the MO/TiO₂/CP (52.8 and 31.5 mF cm⁻²), CM/CP (145.1 and 93.8 mF cm⁻²), and TiO_{2-x}/CP (58.7 and 26.4 mF cm⁻²), confirming the larger electrochemically active surface area of the CM/TiO_{2-x}/CP. Maximized exposure of surfaces ensues increased accessibility of active sites mainly originates from the 3D structural engineering of TiO_{2-x} nanoneedle array with open framework that hosts the homogeneous dispersion of abundant metallic species and N-CNTs, enabling high utilization of catalysts. Additionally, the metallic TiO anchored to carbon paper and wrapped by N-CNTs can provide a highly conductive electron transport channel and facilitate the electron and charge transfer kinetics as validated by the electrochemical impedance spectroscopy (EIS). Figure S20 (Supporting Information) displays the Nyquist plots and corresponding equivalent circuits that consist of a resistor (R_s), as contact resistance, in series with a parallel combination

of a resistor (R_{ct}), as charge transfer resistance, and a constant phase element (CPE). The CM/TiO_{2-x}/CP presents lower R_s and R_{ct} compared with those of MO/TiO₂/CP and CM/CP for both OER and HER processes, demonstrating its favorable electron and charge transfer.

Despite superior light absorption and efficient light-thermal conversion features of the CM/TiO_{2-x}/CP, considerable heat loss at the electrode is inevitable due to its expansive 2D planar figuration, bulk electrolyte medium, and high heat conduction.^[29] This eventually leads to a fast heat transfer from the CM/TiO_{2-x}/CP electrode to electrolyte, and induces massive heat losses around the electrode, thus causing poor photothermal utilization. Considering the strong correlation between heat transfer capacity of electrolyte and temperature gradient across the electrolyzer cell, it is desirable to minimize heat diffusion in electrolyte and create a restricted high temperature region around the working electrode. In this regard, thermal management at the interface of electrode and electrolyte using low intrinsic thermal conductivity, excellent hydrophilicity, low cost, compressible property, and high porosity melamine foam (MF) is adopted.^[52,53] As presented in Figure 4a,b, a piece of MF is placed in a custom designed electrolyzer with a quartz window for light harvesting of the CM/TiO_{2-x}/CP photothermal electrode. Due to capillary effect and macroporous structure of MF with abundant channels for ions transportation, the electrolyte is fully contained and exchanged in the electrolyzer. EIS characterization further shows insignificant influence of MF toward charge transfer resistance (Figure S21, Supporting Information), in which the thickness of the foam is explored and screened. Unlike a free-flowing electrolyte in a conventional electrolyzer cell with smooth and uninterrupted thermal convection, the thermal convection of this cell

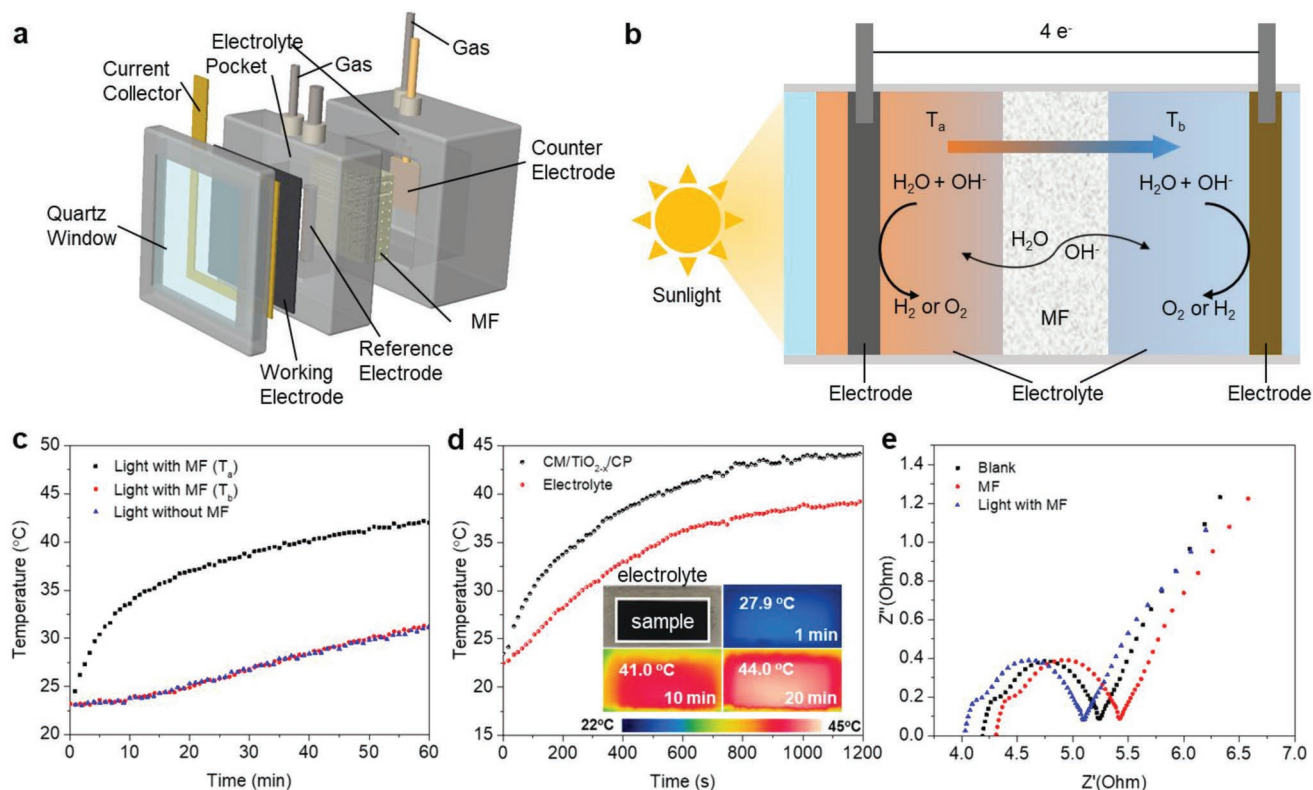


Figure 4. a) The exploded view of the photothermal electrode–electrolyzer. b) Schematic diagram of photothermal electrocatalytic water splitting process of the photothermal electrode–electrolyzer. c) The electrolyte temperature evolution in different part of the electrolyzer, and d) the temperature evolution of the CM/TiO_{2-x}/CP electrode and surrounding electrolyte, (inset: infrared images with marked recorded time and temperature of the electrode) under simulated one sun light irradiation. e) Nyquist plots of CM/TiO_{2-x}/CP recorded at –1.3 V (vs SCE) with/without MF or simulated one sun light irradiation.

design is severely hampered by the insulative reticulated structure of the confined MF subassembly. Consequently, heat loss is effectively suppressed and heat is localized at the perpetually hot zone of the photothermal working electrode, as shown in the diagram of Figure 4b. In order to explore the impact of MF on localized photothermal heating under one sun irradiation, the temperature profiles at different parts of the electrolyte are recorded separately. Upon exposure to irradiation, instantaneous and rapid temperature rise occurs in the T_a area (hot localized zone) from a room temperature of ≈22.8 to 42.5 °C after 60 min (Figure 4c). In contrast, the T_b area (cool zone) and electrolyte without MF show a much slower temperature increase (from 22.8 to 31 °C). This difference evidently confirms that heat localization is achieved via the implementation of insulative MF that is capable of limiting the heat interchange within the electrolyzer cell, the difference depends on the thickness of MF (Figure S22, Supporting Information) and solar intensity (Figure S23, Supporting Information). Figure 4d presents the thermography and infrared images (inset) of the CM/TiO_{2-x}/CP soaked in the MF-electrolyzer under simulated one sun irradiation. Temperature of the CM/TiO_{2-x}/CP (45 °C) is 5 °C higher than the surrounding electrolyte after 20 min, which is anticipated to contribute to the photothermic electrocatalytic water splitting activity of the CM/TiO_{2-x}/CP. Charge transfer resistance measurements (Figure 4e) reveal enhanced conductivity which subsequently lead to improved kinetics reactions.

The CM/TiO_{2-x}/CP photothermal electrode is finally combined with the heat localized electrolyzer to investigate the effect of light-irradiation mediated solar-heat conversion on HER and OER activity. Figure 5a shows comparative polarization plots for CM/TiO_{2-x}/CP that are obtained in simulated one sun irradiation. OER activity is significantly augmented when the CM/TiO_{2-x}/CP is exposed to light radiation with the adoption of MF insulation as evidenced by the positive shift of polarization curve (red line) across all potentials, compared to the absence of MF insulation (blue line) and light-off (black line) condition. These results collectively, suggest the ability of the designed photo-electrocatalytic electrode to absorb broad solar spectrum to generate solar heating or to induce photothermal effect to promote the electrocatalytic process. For instance, at an overpotential of 300 mV, the CM/TiO_{2-x}/CP can reach a current density of 77 mA cm⁻², almost 2.6 times of that measured under light-off condition. Similar HER improvement from 30 to 42 mA cm⁻² at an overpotential of 200 mV can be observed in Figure 5b. Notably, the OER activity is significantly improved due to the photothermal effect as proved by the substantial increase of oxidation peak area around 1.5 V, which should be attributed to the promoted oxidation of nickel-iron species. Previous studies have suggested that for the OER, that involves Ni-based catalysts in alkaline electrolyte, the highly oxidative nickel is identified to be the actual active site.^[54–56] Incremental performance enhancements are reflected by the OER and HER polarization curves (Figure S24, Supporting Information),

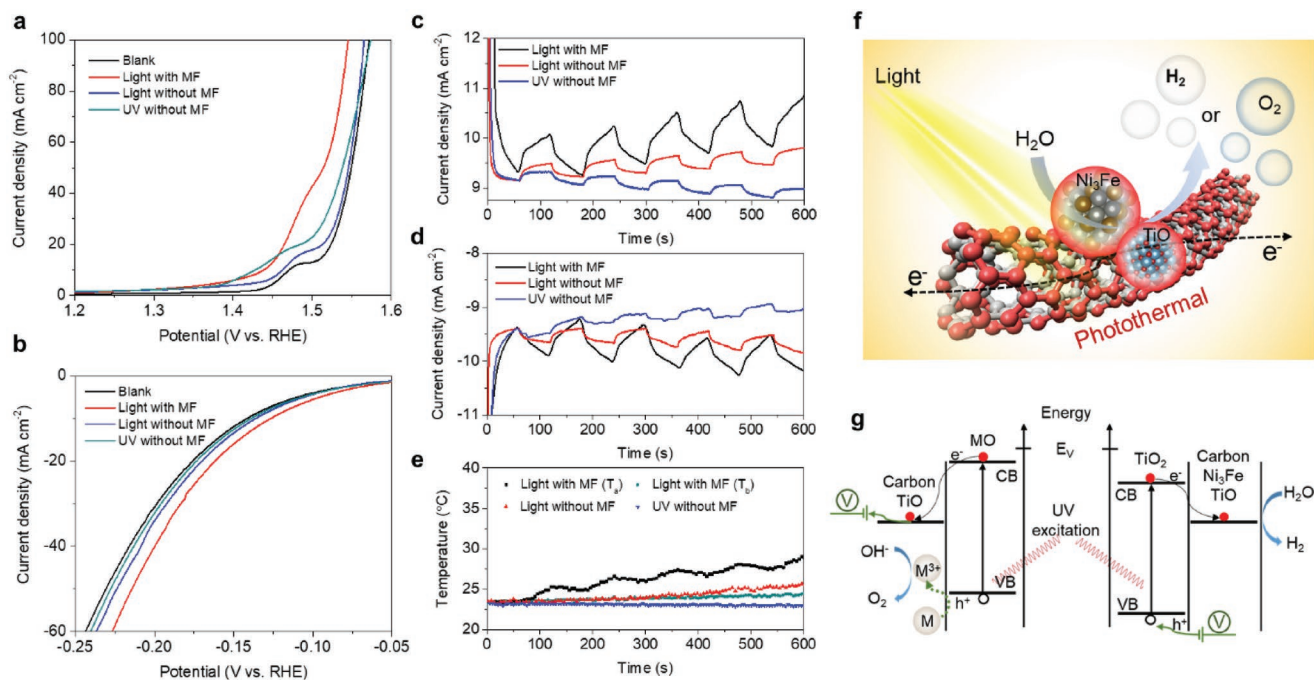


Figure 5. Photothermal electrochemical activities toward OER and HER of CM/TiO_{2-x}/CP. a) OER and b) HER polarization curves with/without MF or simulated one sun light irradiation or UV light. c,d) Chronoamperometric *I*-*T* curves at a bias voltage under chopped illumination for OER (c) and HER (d). e) The corresponding electrolyte temperature evolution. f,g) Schematic illustrations for the proposed photothermal electrocatalytic water splitting mechanism of the CM/TiO_{2-x}/CP electrode–electrolyzer system with photothermal effect (f) and semiconductor-based UV excitation (g).

and gradually reduced impedances (Figure S25, Supporting Information) which closely follow the gradient of luminous intensity, which further proves the photothermal effect. To examine the factor that drives the improvement in HER/OER catalytic activity, chopped illumination under simulated one sun irradiation and UV light was applied to the CM/TiO_{2-x}/CP electrode to obtain chronoamperometric *I*-*T* curve at applied bias. As shown in Figure 5c, the *I*-*T* curve of the CM/TiO_{2-x}/CP electrode in MF confined electrolyte under one sun irradiation has a sawtooth form and an overall upward trend. Upon each repeated on–off cycle, the current density exhibits a rapid and continuous photoresponse with a fluctuation of 1.1 mA cm⁻². For comparison, the CM/TiO_{2-x}/CP shows a lower response to chopped UV (a fluctuation of 0.1 mA cm⁻²) and simulated one sun irradiation without MF (a fluctuation of 0.3 mA cm⁻²). Moreover, upon exposure to UV irradiation on–off cycle, *I*-*T* curves show an overall downward trend in current densities for both HER and OER, and reach a plateau before light-off condition (Figure 5c,d). Impressively, the temperature fluctuation (≈2 °C) of the electrolyte around the CM/TiO_{2-x}/CP electrode (*T*_a) almost synchronizes with the photoresponse of the current density, and both exhibit overall upward trend. By contrast, chopped UV and simulated sun irradiation without MF exhibit negligible or slight temperature change. These experimental results verify that a synergetic effect between the photo-generated carriers from excited semiconductor oxides and photothermal conversion have simultaneously boost the HER and OER performance. The photo to heat conversion will thermally promote dynamics of photo-redox reactivity, which facilitates the separation of photo-generated electron–hole pairs, and accelerate the photoelectron transportation to metallic alloy, TiO and/or carbon for hydrogen evolution, and hole consumption

through the oxidation of Ni and Fe species for oxygen evolution. Meanwhile, the additional photothermal nonradiative thermalization process provides localized heat and boosts reaction kinetics of the electrocatalytic process. Figure 5f,g shows the schematic illustration of the abovementioned synergistic effect for the tailored hybrid photothermal electrocatalytic CM/TiO_{2-x}/CP for efficient photothermic electrocatalytic water splitting.

In summary, we have designed and fabricated a localized photothermic electrocatalytic water splitting system to successfully convert solar energy into chemical fuels. A hybrid carbon/alloy/semiconductor electrode prepared by in situ reduction and CVD strategy is employed as an electrocatalyst material for HER and OER, and its activity is boosted by leveraging its intrinsically high solar absorptivity and light-thermal conversion capability. The CM/TiO_{2-x}/CP electrocatalyst shows low overpotentials, Tafel slopes, high current densities, and long-term stability for both HER and OER in alkaline media assisted by the full solar harvesting and efficient solar–thermal conversion. When applied in a novel electrolyzer design that involves a thermal insulation to suppress immense heat losses and localize the photothermal conversion, the CM/TiO_{2-x}/CP hybrid electrode exhibits a significantly enhanced electrocatalytic performance. The proposed photothermal-assisted approach pioneers a feasible way toward effective harvesting and utilization of sustainable solar energy.

Supporting Information

Supporting Information is available from the Wiley Online Library or from the author.

Acknowledgements

This work was supported by the Ministry of Education Singapore (MOE), R-263-000-D08-114 and R-263-000-D18-112.

Conflict of Interest

The authors declare no conflict of interest.

Keywords

electrocatalytic water splitting, hybrid electrodes, photothermal, thermal localization

Received: June 7, 2019

Revised: July 8, 2019

Published online: July 31, 2019

- [1] W. S. Yang, J. H. Noh, N. J. Jeon, Y. C. Kim, S. Ryu, J. Seo, S. I. Seok, *Science* **2015**, *348*, 1234.
- [2] A. Polman, M. Knight, E. C. Garnett, B. Ehrler, W. C. Sinke, *Science* **2016**, *352*, aad4424.
- [3] W.-J. Ong, L.-L. Tan, Y. H. Ng, S.-T. Yong, S.-P. Chai, *Chem. Rev.* **2016**, *116*, 7159.
- [4] L. Guo, Z. Yang, K. Marcus, Z. Li, B. Luo, L. Zhou, X. Wang, Y. Du, Y. Yang, *Energy Environ. Sci.* **2018**, *11*, 106.
- [5] D. Voiry, H. S. Shin, K. P. Loh, M. Chhowalla, *Nat. Rev. Chem.* **2018**, *2*, 0105.
- [6] I. Roger, M. A. Shipman, M. D. Symes, *Nat. Rev. Chem.* **2017**, *1*, 0003.
- [7] J. W. Ager, M. R. Shaner, K. A. Walczak, I. D. Sharp, S. Ardo, *Energy Environ. Sci.* **2015**, *8*, 2811.
- [8] A. Landman, H. Dotan, G. E. Shter, M. Wullenkord, A. Houaijia, A. Maljusch, G. S. Grader, A. Rothschild, *Nat. Mater.* **2017**, *16*, 646.
- [9] L. Lin, H. Ou, Y. Zhang, X. Wang, *ACS Catal.* **2016**, *6*, 3921.
- [10] J. Luo, J.-H. Im, M. T. Mayer, M. Schreier, M. K. Nazeeruddin, N.-G. Park, S. D. Tilley, H. J. Fan, M. Grätzel, *Science* **2014**, *345*, 1593.
- [11] F. Ning, M. Shao, S. Xu, Y. Fu, R. Zhang, M. Wei, D. G. Evans, X. Duan, *Energy Environ. Sci.* **2016**, *9*, 2633.
- [12] L. Wang, H. Xiao, T. Cheng, Y. Li, W. A. Goddard III, *J. Am. Chem. Soc.* **2018**, *140*, 1994.
- [13] M. R. Nellist, F. A. Laskowski, F. Lin, T. J. Mills, S. W. Boettcher, *Acc. Chem. Res.* **2016**, *49*, 733.
- [14] F. E. Osterloh, *Chem. Soc. Rev.* **2013**, *42*, 2294.
- [15] T. J. Jacobsson, *Energy Environ. Sci.* **2018**, *11*, 1977.
- [16] T. J. Jacobsson, V. Fjällström, M. Edoff, T. Edvinsson, *Sol. Energy Mater. Sol. Cells* **2015**, *138*, 86.
- [17] P. Chen, K. Xu, Z. Fang, Y. Tong, J. Wu, X. Lu, X. Peng, H. Ding, C. Wu, Y. Xie, *Angew. Chem.* **2015**, *127*, 14923.
- [18] F. Song, X. Hu, *Nat. Commun.* **2014**, *5*, 4477.
- [19] C. Tang, N. Cheng, Z. Pu, W. Xing, X. Sun, *Angew. Chem., Int. Ed.* **2015**, *54*, 9351.
- [20] J. Duan, S. Chen, M. Jaroniec, S. Z. Qiao, *ACS Nano* **2015**, *9*, 931.
- [21] C. Niether, S. Faure, A. Bordet, J. Deseure, M. Chatenet, J. Carrey, B. Chaudret, A. Rouet, *Nat. Energy* **2018**, *3*, 476.
- [22] X. Liu, L. Dai, *Nat. Rev. Mater.* **2016**, *1*, 16064.
- [23] M. Ye, J. Jia, Z. Wu, C. Qian, R. Chen, P. G. O'Brien, W. Sun, Y. Dong, G. A. Ozin, *Adv. Energy Mater.* **2017**, *7*, 1601811.
- [24] P. Tao, G. Ni, C. Song, W. Shang, J. Wu, J. Zhu, G. Chen, T. Deng, *Nat. Energy* **2018**, *1*.
- [25] P. Yang, K. Liu, Q. Chen, J. Li, J. Duan, G. Xue, Z. Xu, W. Xie, J. Zhou, *Energy Environ. Sci.* **2017**, *10*, 1923.
- [26] G. Ni, G. Li, S. V. Boriskina, H. Li, W. Yang, T. Zhang, G. Chen, *Nat. Energy* **2016**, *1*, 16126.
- [27] Y. Yang, H. Zhao, Z. Yin, J. Zhao, X. Yin, N. Li, D. Yin, Y. Li, B. Lei, Y. Du, *Mater. Horiz.* **2018**, *5*, 1143.
- [28] W. Xu, X. Hu, S. Zhuang, Y. Wang, X. Li, L. Zhou, S. Zhu, J. Zhu, *Adv. Energy Mater.* **2018**, *8*, 1702884.
- [29] L. Zhu, M. Gao, C. K. N. Peh, X. Wang, G. W. Ho, *Adv. Energy Mater.* **2018**, *8*, 1702149.
- [30] Y. Shi, R. Li, Y. Jin, S. Zhuo, L. Shi, J. Chang, S. Hong, K.-C. Ng, P. Wang, *Joule* **2018**, *2*, 1171.
- [31] X. Hu, W. Xu, L. Zhou, Y. Tan, Y. Wang, S. Zhu, J. Zhu, *Adv. Mater.* **2017**, *29*, 1604031.
- [32] N. Xu, X. Hu, W. Xu, X. Li, L. Zhou, S. Zhu, J. Zhu, *Adv. Mater.* **2017**, *29*, 1606762.
- [33] M. Gao, K. N. C. Peh, L. Zhu, G. W. Ho, *Energy Environ. Sci.* **2019**, *12*, 841.
- [34] T. Li, G. Luo, K. Liu, X. Li, D. Sun, L. Xu, Y. Li, Y. Tang, *Adv. Funct. Mater.* **2018**, *28*, 1805828.
- [35] Z. Li, J. Zhang, B. Guan, D. Wang, L.-M. Liu, X. W. D. Lou, *Nat. Commun.* **2016**, *7*, 13065.
- [36] J. R. Swierk, K. P. Regan, J. Jiang, G. W. Brudvig, C. A. Schmuttenmaer, *ACS Energy Lett.* **2016**, *1*, 603.
- [37] H. X. Zhong, J. Wang, Q. Zhang, F. Meng, D. Bao, T. Liu, X. Y. Yang, Z. W. Chang, J. M. Yan, X. B. Zhang, *Adv. Sustainable Syst.* **2017**, *1*, 1700020.
- [38] Y. Liang, Y. Li, H. Wang, J. Zhou, J. Wang, T. Regier, H. Dai, *Nat. Mater.* **2011**, *10*, 780.
- [39] Y. Hou, Z. Wen, S. Cui, S. Ci, S. Mao, J. Chen, *Adv. Funct. Mater.* **2015**, *25*, 872.
- [40] C. Wang, H. Yang, Y. Zhang, Q. Wang, *Angew. Chem., Int. Ed.* **2019**, *58*, 6099.
- [41] H. Cheng, M. L. Li, C. Y. Su, N. Li, Z. Q. Liu, *Adv. Funct. Mater.* **2017**, *27*, 1701833.
- [42] Y. Yang, Z. Lun, G. Xia, F. Zheng, M. He, Q. Chen, *Energy Environ. Sci.* **2015**, *8*, 3563.
- [43] Y. Chen, S. Choi, D. Su, X. Gao, G. Wang, *Nano Energy* **2018**, *47*, 331.
- [44] J. Xu, D. Wang, H. Yao, K. Bu, J. Pan, J. He, F. Xu, Z. Hong, X. Chen, F. Huang, *Adv. Mater.* **2018**, *30*, 1706240.
- [45] M. Q. Yang, L. Shen, Y. Lu, S. W. Chee, X. Lu, X. Chi, Z. Chen, Q. H. Xu, U. Mirsaidov, G. W. Ho, *Angew. Chem., Int. Ed.* **2019**, *58*, 3077.
- [46] X. Lu, W.-L. Yim, B. H. Suryanto, C. Zhao, *J. Am. Chem. Soc.* **2015**, *137*, 2901.
- [47] I. S. Amiin, Z. Pu, X. Liu, K. A. Owusu, H. G. R. Monestel, F. O. Boakye, H. Zhang, S. Mu, *Adv. Funct. Mater.* **2017**, *27*, 1702300.
- [48] G. Yilmaz, C. F. Tan, Y. F. Lim, G. W. Ho, *Adv. Energy Mater.* **2019**, *9*, 1802983.
- [49] S.-F. Hung, Y.-T. Chan, C.-C. Chang, M.-K. Tsai, Y.-F. Liao, N. Hiraoka, C.-S. Hsu, H. M. Chen, *J. Am. Chem. Soc.* **2018**, *140*, 17263.
- [50] S. F. Hung, Y. Y. Hsu, C. J. Chang, C. S. Hsu, N. T. Suen, T. S. Chan, H. M. Chen, *Adv. Energy Mater.* **2018**, *8*, 1701686.
- [51] H. Wu, X. Lu, G. Zheng, G. W. Ho, *Adv. Energy Mater.* **2018**, *8*, 1702704.
- [52] C. Li, D. Jiang, B. Huo, M. Ding, C. Huang, D. Jia, H. Li, C.-Y. Liu, J. Liu, *Nano Energy* **2019**, *60*, 841.
- [53] C. Li, D. Jiang, H. Liang, B. Huo, C. Liu, W. Yang, J. Liu, *Adv. Funct. Mater.* **2018**, *28*, 1704674.
- [54] H. Zhong, J. Wang, F. Meng, X. Zhang, *Angew. Chem., Int. Ed.* **2016**, *55*, 9937.
- [55] F. Song, M. M. Busch, B. Lassalle-Kaiser, C.-S. Hsu, E. Petkucheva, M. Bensimon, H. M. Chen, C. Corminboeuf, X. Hu, *ACS Cent. Sci.* **2019**, *5*, 558.
- [56] Q. Hu, X. Liu, B. Zhu, L. Fan, X. Chai, Q. Zhang, J. Liu, C. He, Z. Lin, *Nano Energy* **2018**, *50*, 212.